IOP Publishing Journal of Neural Engineering
J. Neural Eng. **15** (2018) 036011 (13pp) https://doi.org/10.1088/1741-2552/aaac39

Optimization of pillar electrodes in subretinal prosthesis for enhanced proximity to target neurons

Thomas Flores[1,6], Xin Lei[2], Tiffany Huang[2], Henri Lorach[3,4], Roopa Dalal[3], Ludwig Galambos[2], Theodore Kamins[2], Keith Mathieson[5] and Daniel Palanker[3,4]

[1] Department of Applied Physics, Stanford University, Stanford, CA, United States of America
[2] Department of Electrical Engineering, Stanford University, Stanford, CA, United States of America
[3] Department of Ophthalmology, Stanford University, Stanford, CA, United States of America
[4] Hansen Experimental Physics Laboratory, Stanford University, Stanford, CA, United States of America
[5] Institute of Photonics, University of Strathclyde, Glasgow, Scotland, United Kingdom

E-mail: tomflo@stanford.edu

Received 16 September 2017, revised 25 January 2018
Accepted for publication 1 February 2018
Published 5 March 2018

Abstract

Objective. High-resolution prosthetic vision requires dense stimulating arrays with small electrodes. However, such miniaturization reduces electrode capacitance and penetration of electric field into tissue. We evaluate potential solutions to these problems with subretinal implants based on utilization of pillar electrodes. *Approach.* To study integration of three-dimensional (3D) implants with retinal tissue, we fabricated arrays with varying pillar diameter, pitch, and height, and implanted beneath the degenerate retina in rats (Royal College of Surgeons, RCS). Tissue integration was evaluated six weeks post-op using histology and whole-mount confocal fluorescence imaging. The electric field generated by various electrode configurations was calculated in COMSOL, and stimulation thresholds assessed using a model of network-mediated retinal response. *Main results.* Retinal tissue migrated into the space between pillars with no visible gliosis in 90% of implanted arrays. Pillars with 10 μm height reached the middle of the inner nuclear layer (INL), while 22 μm pillars reached the upper portion of the INL. Electroplated pillars with dome-shaped caps increase the active electrode surface area. Selective deposition of sputtered iridium oxide onto the cap ensures localization of the current injection to the pillar top, obviating the need to insulate the pillar sidewall. According to computational model, pillars having a cathodic return electrode above the INL and active anodic ring electrode at the surface of the implant would enable six times lower stimulation threshold, compared to planar arrays with circumferential return, but suffer from greater cross-talk between the neighboring pixels. *Significance.* 3D electrodes in subretinal prostheses help reduce electrode-tissue separation and decrease stimulation thresholds to enable smaller pixels, and thereby improve visual acuity of prosthetic vision.

Keywords: retinal degeneration, retinal prosthesis, pillar electrodes, electrical stimulation, neural stimulation, three-dimensional electrodes

(Some figures may appear in colour only in the online journal)

[6] Author to whom any correspondence should be addressed.

1. Introduction

Malfunctioning neural circuits may cause a multitude of debilitating disorders, such as loss of sensory input, impaired motor function, and neurological diseases. The inherent electrical nature of the information encoding in neurons allows treatment of neural disorders by either introducing missing information or inhibiting excessive activity electrically.

Retinal diseases, such as retinitis pigmentosa and age-related macular degeneration, lead to blindness beginning with the progressive loss of photoreceptors [1, 2]. Electronic retinal prostheses aim at restoring sight by reintroducing visual information with electrical stimulating arrays that target surviving retinal neurons. Traditionally, retinal prostheses are divided into three major approaches based on their implantation site [3]. In the epiretinal approach, arrays are implanted on top of the inner limiting membrane (ILM) [4], while subretinal prostheses are located between the inner nuclear layer (INL) and pigmented epithelium [5, 6]. Suprachoroidal prostheses are implanted between the choroid and sclera, and are therefore the farthest removed from the retina [7]. Recent clinical trials of all these systems show some restoration of visual perception, with highest visual acuity reported of 20/1260 [8], 20/550 [9], and 20/4000 [7] for epiretinal, subretinal, and suprachoroidal prostheses, respectively.

Epiretinal prostheses typically directly stimulate the retinal ganglion cells (RGC), with the aim of eliciting a single action potential in response to a single pulse of current. This allows visual information to be encoded in a digital format by controlling the timing and number of spikes. Ideally, it may allow reproducing a natural retinal code if the proper pulse sequences are generated from the captured video stream and delivered selectively to various types of the RGCs [10]. A major problem with the epiretinal approach is the inability to stimulate single RGCs without eliciting responses from the nearby passing axons originating in remote cells. Such axonal stimulation causes arcuate percepts that strongly distort the retinotopic map [11].

Subretinal implants stimulate the nearby bipolar cells, which then lead to spiking of RGCs via the retinal neural network. The graded-response (non-spiking) neurons in the INL (bipolar, horizontal and amacrine cells) allow for modulation of their response by adjusting the amplitude and duration of the stimulus—an analogue interface, as opposed to a digital (binary) encoding in direct stimulation of RGCs. This approach, relying on the remaining retinal neural network, was shown to preserve multiple features of the natural retinal signal processing, including flicker fusion, adaptation to static images, antagonistic center-surround, as well as linear and non-linear summation of subunits in the RGC receptive fields, which enables high spatial resolution [6]. The slower nature of non-spiking neurons allows stimulation with much longer pulses than RGCs (1–10 ms, as opposed to 0.1–0.5 ms), which helps reduce their stimulation thresholds [12], and thereby avoids direct activation of RGCs and their axons. Interestingly, this effect can be utilized also by the epiretinal implants, and axonal stimulation can be avoided if RGCs are activated indirectly, via bipolar cells, with pulse durations exceeding 25 ms [13].

Stimulation of neural circuitry with high spatial resolution requires localization of electric fields produced by the stimulating electrodes. Separation between electrodes and tissue leads to the loss of spatial confinement. Multiple electrodes may therefore affect a single neuron (electrical cross-talk), which will reduce the resolution and contrast of the stimulating patterns [14]. To prevent significant lateral spread of electric field, the distance to the target neurons should not exceed the pixel radius. Normal 20/20 visual acuity corresponds to resolving a grating of 10 μm period on the retina [15], and requires pixel size of no larger than 5 μm for adequate sampling. For 20/200 visual acuity, defined as a threshold of legal blindness in the US, pixel size must be smaller than 50 μm. Recent measurements of prosthetic visual acuity with 70 μm subretinal photovoltaic pixels in rats confirmed that acuity is currently limited by the pixel pitch [6]. Stronger dependence of the stimulation threshold on separation between smaller electrodes and neurons, higher electrode access resistance, and reduced capacitance are all problematic for higher-resolution prostheses.

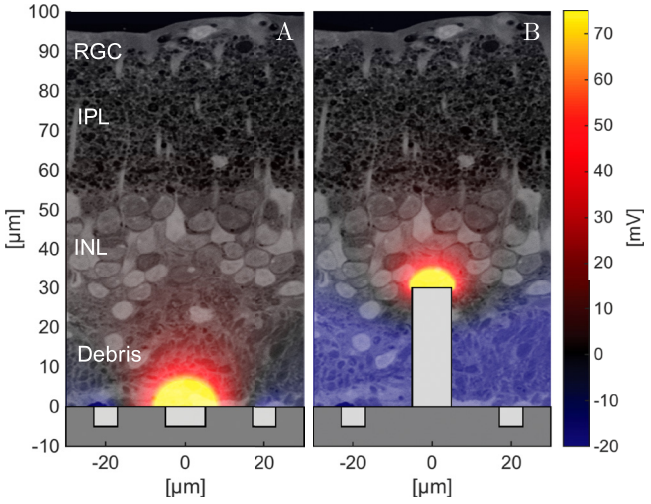

Figure 1. Motivation for a 3D subretinal prosthesis. Degenerated RCS retinas exhibit near complete loss of photoreceptors at P120, which are replaced by debris (≈30 μm thick), separating the inner nuclear layer (INL) from RPE. Such separation between the subretinal electrodes and target neurons in INL reduces stimulation efficacy (A). Pillar electrodes (30 μm tall) can bypass debris and more effectively deliver electric field to the target cells (B).

Three-dimensional (3D) implants have been proposed to reduce separation between electrodes and cells, as illustrated in figure 1. While epiretinal structures [16–18] require mechanical pressure for achieving close proximity to RGCs, subretinal arrays reduce this distance by allowing migration of cells into the open space in the 3D implant [19]. Both protruding [15, 20] and recessed [21, 22] electrodes have been shown to reduce the separation between electrodes and INL by utilizing retinal migration. Penetrating, rather than recessed, structures additionally allow increasing the electrode surface area, which improves capacitance and reduces the electrode access resistance [18, 23, 24].

In this study, we evaluate the optimal design of pillar electrodes on subretinal implants with respect to anatomical integration and stimulation capabilities. In search of the optimal electrode configuration, we model electric fields using 3D finite element analysis, and quantify retinal activation using a model of network-mediated stimulation. We assessed

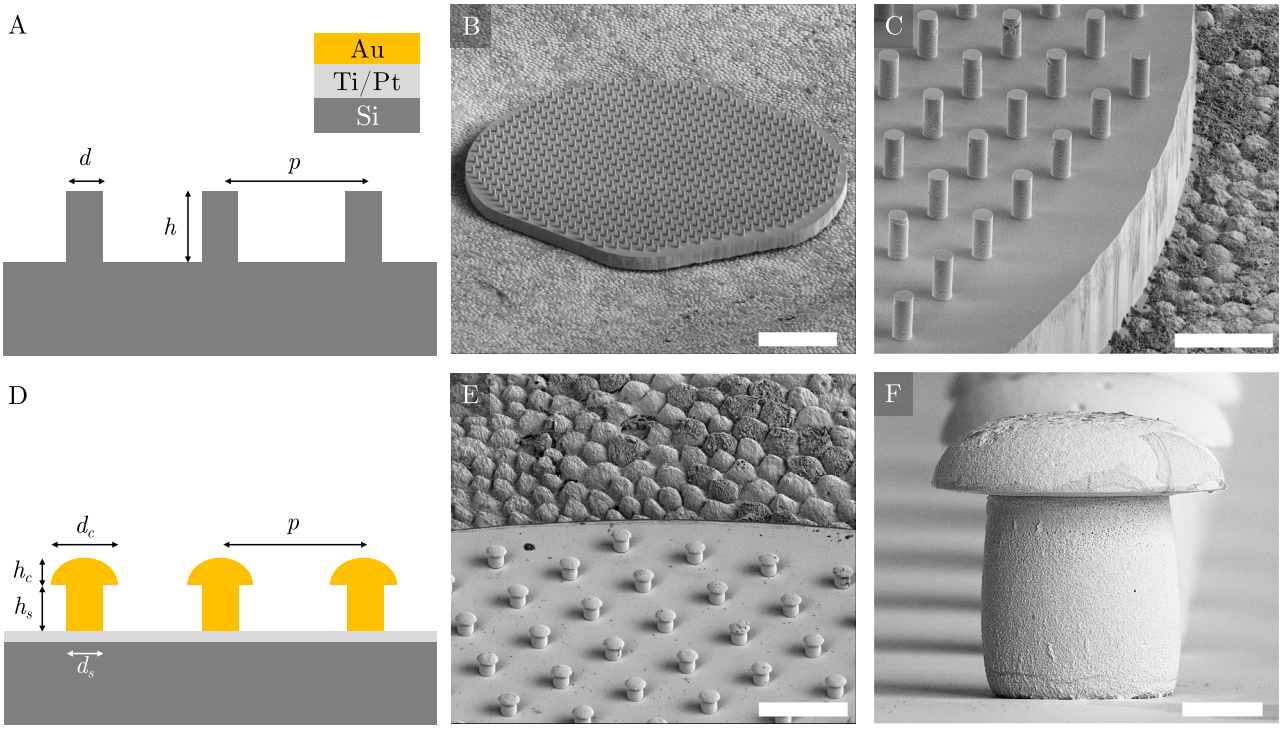

Figure 2. Pillar arrays made of silicon ((A)–(C)) and electrodeposited gold ((D)–(F)) were fabricated to study integration with the retina. Silicon base is 1 mm in diameter and 40 μm in thickness. (A) Diagram of silicon devices with various pillar diameters (d), heights (h) and pitch (p). (B) SEM image of a subretinal implant with pillars $h = 22$ μm, $d = 6$ μm, and $p = 40$ μm. (C) Higher magnification of the same array. D) Electrodeposited pillar consists of a stem with diameter d_s with height h_s and ellipsoidal cap with diameter d_c and height h_c. (E) Implant with electrodeposited pillars: $p = 40$ μm, $d_s = 6$ μm, $h_s = 7$ μm, $d_c = 10$ μm, and $h_c = 3$ μm. (F) Higher magnification view of the same. All SEM images taken with implant placed on porcine RPE. Scale bars = 200 μm (B), 40 μm (C), 40 μm(E), and 3 μm (F).

anatomical integration using confocal imaging of the whole mount retina with the implant, and developed a procedure for sectioning implanted retinas for histology. Finally, we developed a fabrication process of the pillar electrodes on top of photovoltaic arrays using electroplating, which allows increasing the surface area and is compatible with device fabrication and deposition of sputtered iridium oxide films (SIROF).

2. Methods

2.1. Subretinal implants

Two types of pillars were fabricated on silicon subretinal implants for this study: (1) silicon pillars, and (2) electroplated gold pillars.

Devices were fabricated from crystalline silicon wafers using two mask layers to generate patterns for deep silicon etching (DSE). A hexamethyldisilizane (HMDS) primed wafer was spin-coated with 4 μm of photoresist (Shipley PR 220-3) and processed to define the pillar regions. A Bosch silicon etch produced the pillars by etching away the exposed silicon regions. After the pillar defining resist was removed, a 5 μm thick layer of photoresist (7.5% Shipley 220-7, 68% MEK, 24.5% PGMEA) was spray-coated over the wafer and pillar surfaces, and processed to define the releasing trenches. A second Bosch process etched 40 μm of silicon to define the releasing trenches, after which the photoresist was removed. To release devices from the wafer, we first spray-coated a 60 μm thick photoresist to protect the front side of the wafer. A backside grinding process (Grinding and Dicing Services, Inc., San Jose, CA, USA) thinned the wafer from 500 μm to 50 μm thickness from the base of the pillar. A XeF_2 gaseous etch then removed the remaining excess silicon to obtain a 40 μm thick device. Finally, the devices were released from the protective photoresist using a heated solvent bath.

A total of nine device configurations with silicon pillars were fabricated, with geometries summarized in figures 2(A)–(C). Pillar heights were $h = 6$ μm, 8.2 μm, or 22 μm. For all heights, pillars had diameter $d = 6$ μm, 10 μm, or 14 μm with pitch $p = 40$ μm, 55 μm, or 70 μm, respectively. Pixel pitch was chosen to reflect our prosthesis designs. In a hexagonal array, they correspond to the sampling density limit for grating visual acuity of up to 20/140, 20/190, and 20/240, respectively. All devices included a 40 μm thick, 1 mm diameter silicon base.

Gold pillars were fabricated using electroplating. Oxidized silicon wafers were first coated with a conductive Ti/Pt seed layer (15 nm and 100 nm, respectively). A 7 μm thick, spin-coated photoresist (Shipley SPR220-7) was then exposed and developed to create vias for electroplating. Gold was deposited using a gold-sulfite based solution (BDT-510; MacDermid Enthone, Waterbury, CT, USA) heated to 50 °C, with DC current density of 12 mA cm^{-2}. Height of the deposition and formation of a cap above the photoresist was monitored via chronovoltammetry [25]. After removing the photoresist, a

7 μm spray-coated resist was patterned to define the releasing trench. The Ti/Pt seed layer and surface oxide were removed using reactive ion and plasma etching, respectively, to expose the underlying silicon. Completion of the releasing trench and subsequent release of the implants were performed as described above for silicon pillar devices.

The electroplated pillars consisted of two distinct regions—a cylindrical stem and rounded cap, as shown in figures 2(D)–(F). Pillars were fabricated with stem height $h_s = 7$ μm, stem diameter $d_s = 6$ μm, cap diameter $d_c = 10$ μm, cap height $h_c = 3$ μm, and pitch $p = 40$ μm. The released devices contained a 40 μm, 1 mm diameter silicon base.

2.2. SIROF coating of pillar surface

Stimulating electrodes must operate within the electrochemical water window (-0.6 V $< V_{\text{electrode}} < 0.8$ V) to avoid inducing irreversible redox damage to the surrounding tissue and electrode material. The performance of electro-neural interfaces is therefore limited by the charge injection capacity (CIC) of the electrode material to allow for adequate current injection within this range of voltages. We use SIROF in our photovoltaic prostheses due to its high CIC (>1 mC cm^{-2}) compared to polished metal (≈0.01 mC cm^{-2}) [26, 27]. 3D electrodes must therefore be fabricated in a way that allows for the deposition of SIROF on their surface. To maximize the electric potential drop across the target cell layer, SIROF should be deposited only on top of the pillar electrode. On electrodes coated with various materials, current density in steady state (typically reached within sub-ms duration) is proportional to capacitance per unit area [28]. Therefore, current density injected through the SIROF coating on top of the pillars will be at least 100 times higher than on the gold side walls of the pillar stem. For this reason, there is no need for insulation of its sidewalls—they will deliver negligible current, even if left exposed. This feature greatly simplifies the fabrication of the pillar electrodes.

For selective SIROF deposition on top of the pillars, a 4 μm thick photoresist (Shipley SPR220-7) was spin-coated over the wafer after electroplating, as shown in figure 7(A). We exposed and developed the photoresist on top of the rounded top surface of the pillar to ensure its metal surface is exposed. After deposition of SIROF (EIC Laboratories, Norwood, MA, USA), remaining photoresist was removed from the wafer. The SIROF layer on the pillars was then assessed using focused ion beam sectioning and scanning electron microscopy (FIB-SEM).

2.3. Surgical procedure

All experimental procedures were conducted in accordance with institutional guidelines and the ARVO Statement for the Use of Animals in Ophthalmic and Vision Research. Animal care and subsequent implantation were conducted as previously described [6, 29, 30] using rats with retinal degeneration from a Royal College of Surgeons (RCS) colony maintained at the Stanford Animal Facility. $N = 22$ animals were used in this study, implanted between P180 and P200, when the outer nuclear layer has disappeared. Animals were anesthetized with a mixture of ketamine (75 mg kg^{-1}) and xylazine (5 mg kg^{-1}) injected intramuscularly. A 1.5 mm incision was made through the sclera and choroid 1.5 mm posterior to the limbus. The retina was lifted with an injection of saline solution, and the implant was inserted into the subretinal space. The sclera and conjunctiva were sutured with nylon 10–0, and topical antibiotic (bacitracin/polymyxin B) was applied on the eye postoperatively. Surgical success and retinal reattachment were verified using optical coherence tomography (OCT) (HRA2-Spectralis; Heidelberg Engineering, Heidelberg, Germany). The animals were euthanized six weeks after implantation.

2.4. Whole-mount retinal imaging

Animals were euthanized with an intracardiac injection of Beuthanesia, and eyes were enucleated and rinsed in phosphate buffered saline (PBS). Anterior segment and lens were removed, and upon locating the implant under stereo microscope, the eye cup was cut to a 5 mm × 5 mm square centered around the implant, and fixed in 4% paraformaldehyde (PFA) for one hour at room temperature. The implant was kept in place to prevent tissue damage or reorganization due to its removal. Samples were washed with PBS three times and put in 5% bovine serum albumin (BSA) for 48 h at 4 °C, rinsed three times in PBS, transferred into 0.025% DAPI for 48 h, and covered with Vectashield (H-1000; Vector Laboratories, Burlingame, CA, USA).

3D imaging was performed using a Zeiss LSM 780 confocal inverted microscope with Zeiss ZEN black software. The XY acquisition area was defined to include a minimum of three parallel rows of pillars across the middle of the device. Image tiling and subsequent stitching within the Zen black software was necessary to acquire complete 1 mm long rows of pillars. Image planes were acquired through the total thickness of the retina using a Z-stack with upper and lower bounds defined at the inner limiting membrane (ILM) and 20 μm below the base of the pillars, respectively.

2.5. Image analysis

Confocal datasets were analyzed using the FiJi distribution of ImageJ [31]. Quantification of the implant integration in subretinal space was based on analysis of the cell density. For image analysis, we first maximized the contrast in the individual XY planes to ensure 0.3% channel saturation to correct for brightness variations at different Z positions in the stack. Second, the XY planes were despeckled, and background subtracted. Third, a Gaussian blur filter ($\sigma = 3$ pixels) was applied to smoothen brightness variations within individual cells. Finally, the channel threshold was adjusted (default method) to provide a binary representation of the cells. Fraction of the area occupied by cells in each XY plane was then computed, taking into account the area occupied by the pillars. Implant integration was quantified using three metrics relevant for electrical stimulation of the retina: ratio of cell density at the electrode surface to maximum density in the INL, percent of INL above the electrode surface, and the

distance from electrode surface to region of maximum cell density in the INL.

2.6. Histological sectioning

Following fluorescence imaging, samples were rinsed in buffer and fixed in 1.25% glutaraldehyde solution for 24 h at room temperature. They were then post-fixed in osmium tetroxide for 2 h at room temperature, dehydrated in graded alcohol and propylene oxide. Samples were infiltrated overnight in epoxy (without DMP-30) at room temperature, embedded in epoxy (electron microscopy sciences—Araldite-EMbed, RT13940, Mollenhauer's kit), and baked for 36 h at 70 °C. Epoxy blocks were then trimmed until silicon implants were exposed. To prevent knife damage while sectioning, silicon implants were removed using a XeF_2 etch (Xactix e-1, 23 °C, 3 Torr) for 100 cycles. Blocks were refilled with epoxy by putting them in a vacuum desiccator for 2 h and then left in oven overnight at 70 °C. Thus, empty space after removal of implant was filled with epoxy to provide structural support during sectioning. 700 nm thick sections were then taken using Reichart UltracutE and stained with toluidine blue for light microscopy.

XeF_2 etching did not damage the embedded tissue, while epoxy refilling completely filled the resulting cavity. Gold electrodeposited pillars and the metallic seed layer were left in the blocks prior to sectioning, as these materials did not damage the knife. Wet etchants of metal (KI, Aqua Regea, and H_2O_2+HNO_3) significantly altered both the epoxy and embedded tissue, and were therefore avoided.

2.7. Modeling the electric field and retinal stimulation

Electric field in electrolyte was calculated using a finite element model of the array in COMSOL Multiphysics 5.0, using the electrostatics module. The modeled arrays are 1 mm in diameter, 30 μm thick, and are composed of 502 hexagonal pixels of 40 μm in width, corresponding to our recently fabricated, high-resolution arrays and test implants (figure 2). Electric field is calculated in a volume (cube, side = 10 mm) for which the ground (0 potential) is defined at the periphery. The modeled prosthesis functions as a closed system, in which all the injected current is collected on the device. Electric boundary conditions on electrode surfaces were defined as uniform current density. With electrodes composed of different materials, such as gold stems and SIROF-coated caps of the electroplated electrodes, current density was assumed to be proportional to the capacitance per unit area [28]. Alternating rows of electrodes are activated with 100% contrast by projecting grating patterns, similar to the protocol for assessment of the spatial resolution of prosthetic vision *in vivo* [6, 32]. Photocurrent in each pixel is calculated by multiplying the laser irradiance by the previously measured light-to-current conversion of our photodiodes (0.36A W^{-1}) [33] and the exposed photosensitive area per diode (419 μm) for a two-diode, 40 μm pixel.

Latency of the retinal ganglion cells response to subretinal stimulation (10–50 ms) observed *ex vivo*, indicates that the response is network-mediated [6, 20]. To assess the retinal stimulation characteristics of arrays with various

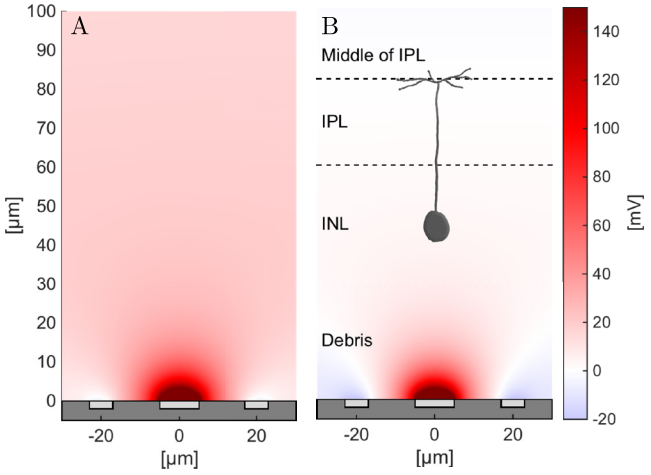

Figure 3. (A) Electric potential distribution in front of a pixel with anodic active electrode 10 μm in diameter, surrounded by a circumferential return electrode of 40 μm in diameter, in electrolyte, for 1 μA current injection. (B) Cells in electric field polarize according to the potential difference across their length. Bipolar cell somas and axon terminals reside in the INL and IPL, respectively. Electric potential is therefore represented with respect to potential in the middle of IPL.

electrode configurations, we assumed that the network-mediated stimulation threshold is defined by a voltage drop across bipolar cells [34], as shown in figure 3. In an external electric field, the intracellular medium becomes equipotential within a microsecond, resulting in hyperpolarization and depolarization of the cell membrane near and far from the anode, respectively [3, 35]. Using the retinal network-mediated stimulation threshold current density for large electrodes (i.e. uniform electric field) with 4 ms pulses from literature ($j = 23$ A m^{-2}) [36], average resistivity of the retina ($\rho = 500\ \Omega$cm), and a mean length of bipolar cells estimated as the distance from the middle of INL to middle of IPL ($L = 37\ \mu$m), we calculated a potential difference threshold (V_{th}) of 4.3 mV from soma to axonal terminals for anodic stimulation.

$$V_{th} = j \cdot \rho \cdot L = 4.3\ \text{mV} \quad (1)$$

The cathodic threshold of −18.9 mV was calculated based on the network-mediated activation curve measured in rat retinas with anodic and cathodic stimulation [6, 20], which was scaled to match the calculated anodic threshold [28].

Assuming that, on average, bipolar cell axons terminate in the middle of the IPL, we found the boundary within which potential difference from the middle of IPL is above the threshold. One measure of the stimulation efficacy can be a fraction of the INL volume per pixel above this threshold. Strength of the neural response also increases with the depolarization voltage, but since this function for a single bipolar cell activation is not well established, and is likely to vary between neuron types, we refrained from a quantitative assessment of the total spiking rate. To study the effects of variable electrode-tissue proximity, as could be affected by cellular debris in the subretinal space, we introduced a separation layer of the same conductivity and variable thickness between the INL and the electrode surface ('Debris' in figure 3), and

compared performance of planar and pillar electrodes of various configurations.

It is important to note that our model is based on the stimulation current densities from the literature, while the calculated trans-cellular voltage scales linearly with the retinal resistivity (equation (1)), for which there is no consensus in the literature [37–39]. We use the trans-cellular voltage only as a means for assessing the boundaries of the activation zone in tissue, relative to the stimulation threshold. Any variation in assumed retinal resistivity linearly affects the potential for the same current, including the threshold potential. Therefore, these variations do not affect the boundaries of the activation zone since they are calculated relative to the stimulation threshold. However, variations in the assumed mean bipolar cell length will linearly affect the calculated threshold potential in a uniform electric field (equation (1)), which will affect the activation volume.

We studied two electrode configurations with pillars: (1) active electrode on top of the pillar and circumferential return at the base, and (2) active electrode configured as a ring at the base, and return electrode on top of the pillar (figure 9). In both cases, active electrode is always considered an anode, and return is always a cathode when light is ON (stimulation phase). The active pillar design resembles our existing prosthesis with connected local returns [28], only with its central electrode elevated into the INL. The return pillar design maximizes the vertical dipole, increasing the voltage step across the cells in the INL. Placement of the ring electrode underneath the cap was chosen for two reasons: (1) photosensitive areas shadowed by the overhanging cap do not contribute any current and are therefore best suited for opaque electrodes, and (2) to maintain at least some spatial confinement of electric field without circumferential local return, the active electrode should be positioned close to the pixel center. For both designs, area of the return electrode was four times larger than that of the active to minimize the current density and associated voltage drop on the return.

3. Results

3.1. Anatomical integration

RCS rats (P180-200, $n = 22$) were implanted with the different pillar arrays in the subretinal space for six weeks (see Methods). Integration of the implants with retinal tissue was monitored *in vivo* by optical coherence tomography (figure 4(A)), and demonstrated stable integration within two to three weeks post implantation.

After six weeks, retinas with implants were imaged *ex vivo* at higher magnification. Optical images of the histological sections of RCS retina with 22 μm tall silicon pillars of 10 μm diameter figure 4(B) and 10 μm tall electroplated pillars figure 4(C) six weeks after implantation are shown in figures 4(B) and (C). In these preparations, the silicon has been removed and refilled with epoxy prior to thin sectioning, while the gold pillars were left intact. Successful, atraumatic implantation enables migration of the INL cells into the gaps between the subretinal pillars of both materials, without gliosis or fibrosis.

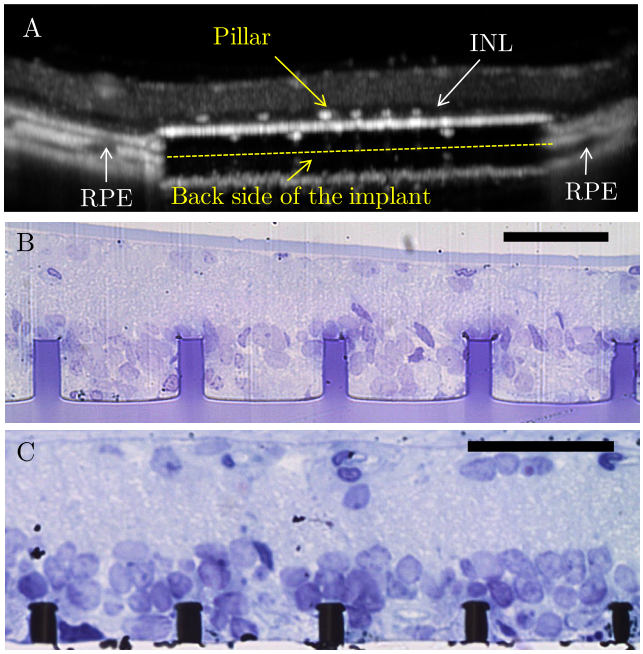

Figure 4. Subretinal implants in RCS rats. (A) OCT image of the implant with pillars ($h = 22$ μm, $d = 14$ μm, $p = 70$ μm) penetrating into the inner nuclear layer. Implant thickness appears 2.3 times greater than in reality (40 μm) due to higher refractive index of Si compared to that of tissue. ((B) and (C)) Histology of the retina demonstrating integration of the pillars with tissue without fibrosis. (B) Silicon implant, $h = 22$ μm, $d = 10$ μm, $p = 55$ μm. Silicon has been etched post fixation and resulting cavities refilled with epoxy. (C) Gold-electroplated pillars on top of the Pt/Ti seed layer were sectioned as is. Scale bars = 40 μm.

Tissue fills the space between the pillars, with some somas reaching the base of the device and others touching the pillar surface. For 22 μm tall pillars, their top surface remains within the INL, but with only one or two cells above the pillar.

In 2/22 animals, traumatic implantations did induce gliosis around the implant. This occurred when the pillars caught the retina during insertion. Fibrotic encapsulation of the implant separated the pillar surface from the INL, and ultimately negated the benefit of the 3D interface. More importantly, such encapsulation surrounded the pillars with a highly resistive tissue that may impede stimulation by limiting or redirecting the injected current away from the target cell layer [40]. Those two samples were excluded from our subsequent image analysis. *Ex vivo* imaging of the implanted retina was also performed in a whole-mount preparation, using confocal fluorescence microscopy (DAPI staining, see Methods). Figure 5 shows the cross sections for the central rows of the confocal stacks obtained with flat implants (A), and 40 μm 3D implants with pillar heights 8.2 μm (B) and 22 μm (C), as well as 10 μm tall electroplated pillars (EP, D). Cell nuclei (DAPI) are represented in yellow for improved visibility on dark background. Color representation inside the opaque silicon pillar is obtained by projecting the imaged surface through the stack. Cross sections represent maximum projection over 3 μm thickness to better detect cells and reduce noise. Since the metal is opaque for light microscopy, confocal image of electroplated pillars represents the width of the electrode cap rather than its narrower stem.

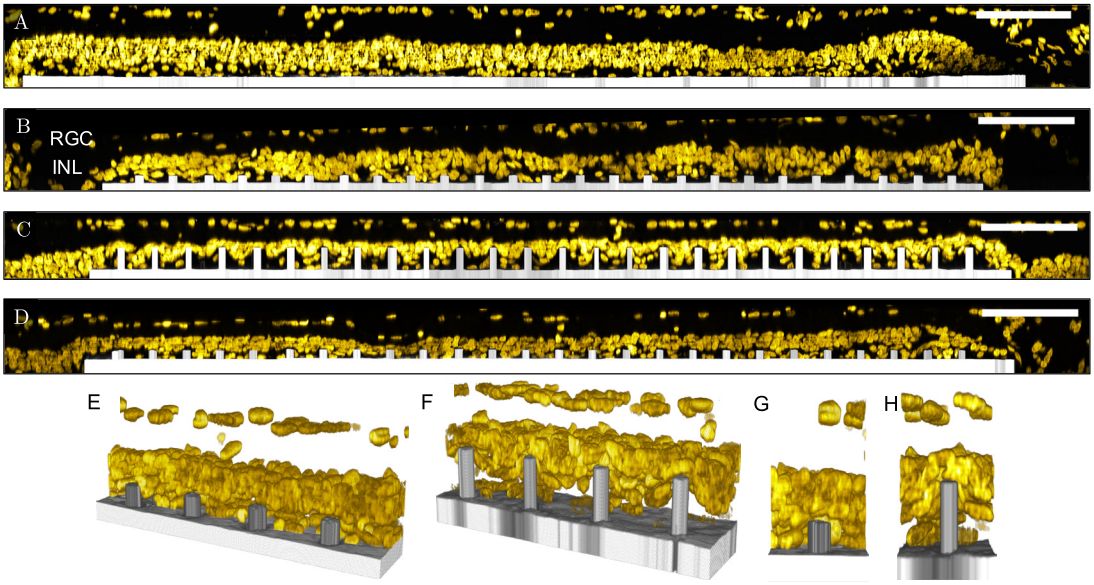

Figure 5. Implant integration with the retina. ((A)–(D)) Confocal images for flat implant (A), implant with silicon pillars of $d = 6$ μm, $p = 40$ μm and $h = 8.2$ μm (B), and $h = 22$ μm (C), and electroplated pillars (D). DAPI stain shown in yellow, projection of the implant surface shown in gray. Scale bar 100 μm. Pillars terminate in the cell-dense regions, with 8.2 μm and 22 μm pillars reaching the lower and upper portion of the INL, respectively. ((E) and (F)) 3D magnified view of electroplated pillars (E) and $h = 22$ μm silicon pillars (F). Cells shown from the middle of pillar to $y = 25$ μm. ((G) and (H)) Profile view of a single electroplated pillar (G) and $h = 22$ μm silicon pillar (H).

Separation between the electrodes and cells in the INL ranges from 0 to about 20 μm with flat implants, but practically disappears with pillars. In these implants, cells migrated toward the base of the pillars, thereby closing the gap between electrodes and cells in the INL. Penetration of the 10 μm tall electroplated and 22 μm tall silicon pillars into the INL is further shown in 3D rendering in figures 5(E)–(H). The 10 μm high pillars penetrate into the lower portion of the INL, with only one cell soma residing below the dome (E, G), while taller pillars induce more robust migration, with multiple rows of somas moving below the pillar upper surface (F, H). For our analysis of the integration of the implanted devices with the retina (figure 6), we quantify three parameters expected to be important for electrical stimulation: cell density at the electrode upper surface relative to the maximum in the INL (D), percent of INL remaining above the electrode upper surface (E), and the distance from electrode surface to the region of maximum cell density in INL (F). Cell density at the electrode upper surface increases with pillar height, with relative densities of 0.11, 0.26, 0.61, 0.84, and 0.96 for $h = 0$ (flat), 6 μm, 8.2 μm, 10 μm, and 22 μm, respectively (figure 6(D)). Percentage of INL above the electrodes decreases with increasing heights, with 89%, 85%, 70%, and 40% of the INL remaining above the pillar upper surface for $h = 6$ μm, 8.2 μm, 10 μm, and 22 μm, respectively (figure 6(E)). The flat array has 100% of INL above the electrode surface by definition. Increasing pillar height reduces the distance between the electrode upper surface and region of maximum INL density, with 27 μm, 28 μm, 17 μm, 6 μm and 1 μm for $h = 6$ μm, 8.2 μm, 10 μm, and 22 μm, respectively (figure 6(F)). For one of the implants with 22 μm pillars, the region of maximum cell density was below the upper surface of several electrodes.

3.2. SIROF coating on electroplated pillars

Based on the electroplated pillar geometry, we developed a SIROF coating method allowing high charge injection capability localized in the INL. SIROF coating of only top of the pillar, as shown in figure 7, rather than the whole 3D structure as previously performed [24] ensures current injection predominately from the region of high CIC in steady state [28]. Since SIROF capacitance per unit area is about 100 times higher than that of gold (1 mF cm^{-2} versus 10 μF cm^{-2}), only 1% of current density will be injected from the pillar sidewalls. Consequently, no insulation is required for the side walls, which greatly simplifies the fabrication process.

Electroplated pillars coated with SIROF are shown in figure 7. Spin-coating the photoresist on a surface with pillars resulted in a sloped-profile at the pillar stem (figure 7(A)). This elevated region of resist worked in conjunction with the overhung cap to prevent SIROF deposition on pillar sidewalls. Lack of SIROF under the cap edge allowed for clear lift-off using chemical solvents.

As shown in figures 7(B) and (C), this process resulted in complete SIROF coverage of the rounded cap, with no SIROF present on the stem walls. Note that the top dark layer in figures 7(C) and (D) represents platinum deposited during the focused ion beam (FIB) milling for cross-sectional view. Morphology of the SIROF film varies across the upper surface, with large grains and lower thickness in the regions

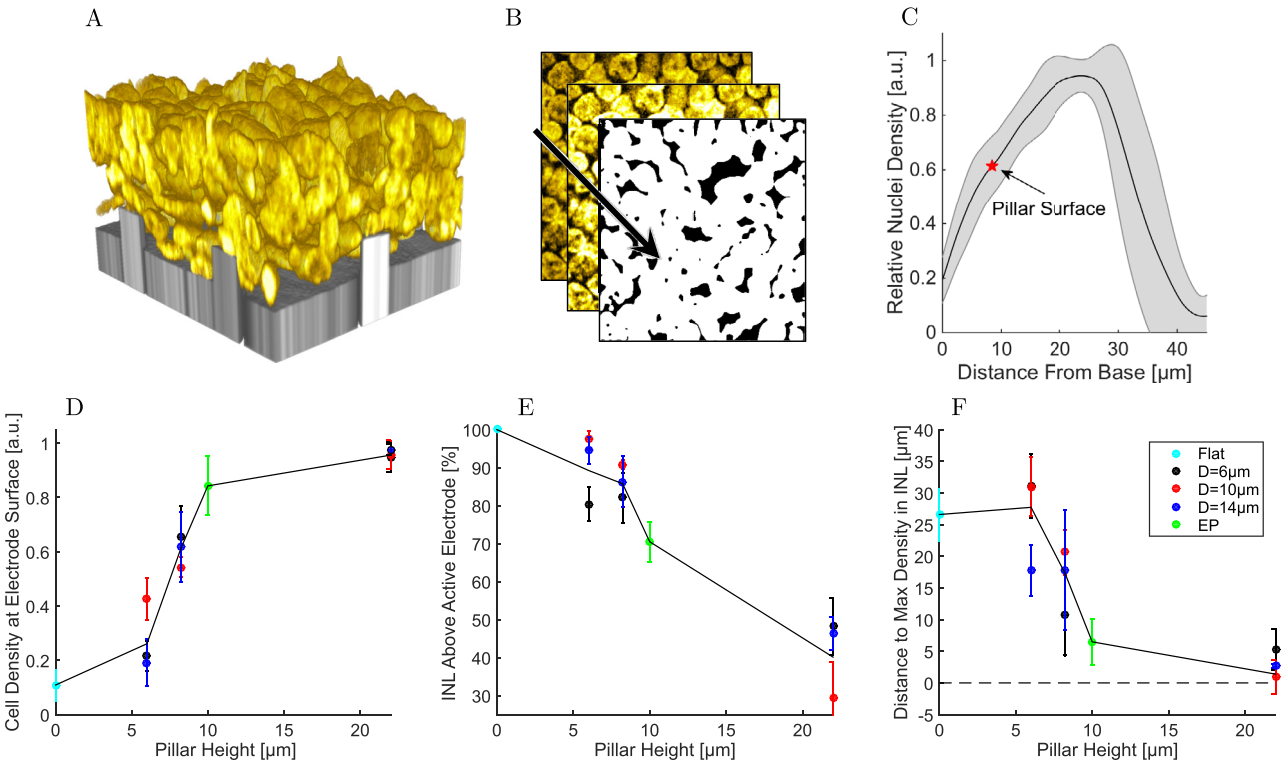

Figure 6. Analysis of the tissue integration. ((A)–(C)) Processing of the confocal image stacks to analyze pillar integration for $h = 8.2$ μm, $d = 6$ μm array. (A) Sub-volume from a confocal stack containing complete INL (yellow) and multiple pillars (gray). (B) Image processing prepares the 3D stack for binary thresholding to calculate the fraction of area occupied by cells in each XY plane. (C) Cell density in all XY planes with respect to maximum density in the stack, as a function of distance from the pillar base. Solid and shaded lines represent the mean and standard deviation of array sub-volumes, respectively. Marker indicates pillar surface. ((D)–(F)) Integration analysis for silicon and electroplated pillar (EP) arrays. Data points represent the mean from two devices of same size. With increasing pillar height, cell density at the pillar surface increases (D), while amount of tissue above the surface (E) and distance to the region of maximum density (F) are decreasing. Solid line connects the weighted mean for each pillar height.

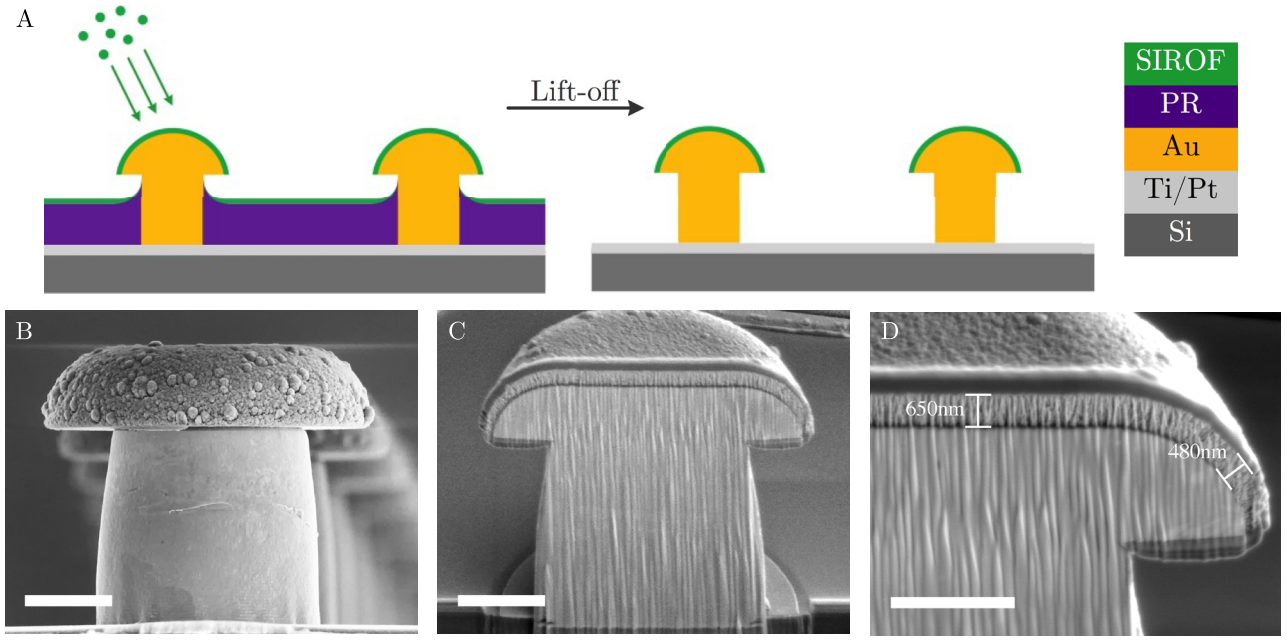

Figure 7. Gold electrodeposited pillars with SIROF-coated top of the dome. (A) SIROF deposition. A spin-coated, 4 μm thick photoresist covers the device and pillar sidewalls, leaving the cap uncovered. Cap overhang prevents SIROF deposition on resist covering the sidewalls. A subsequent lift-off step leaves pillars with SIROF deposits only on caps. (B) Side view of a gold pillar with SIROF coated cap. Deposited SIROF exhibits granularity despite smooth gold electroplating. Scale bar = 3 μm. (C) Cross sectional image of a pillar after FIB milling. Absence of a porous layer on pillar sidewall indicates absence of SIROF. Structure was sputter-coated with platinum during milling (top dark layer). Image tilted to 51°, scale bar = 3 μm. (D) High magnification view showing decrease of the SIROF thickness at curved regions of the cap due to angular deposition. Scale bar = 2 μm.

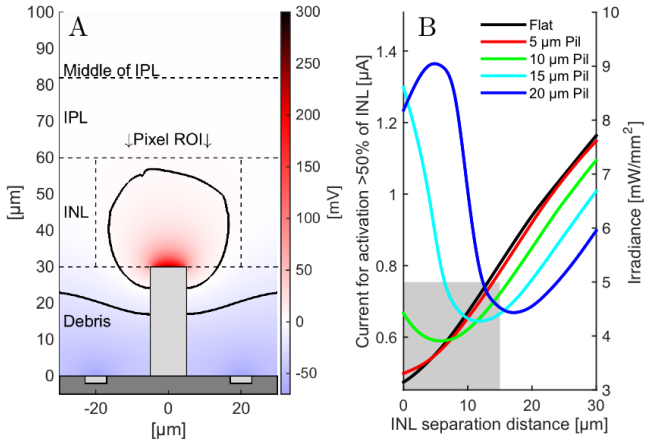

Figure 8. (A) Electric potential for a 30 μm tall pillar electrode with 30 μm thick debris and 1 μA current injection. Pixel region of interest is defined within the pixel width, between the upper and lower INL bounds. Volume above activation thresholds (anodic and cathodic) outlined by black contours. (B) Current and irradiance required for activation of 50% of the INL volume above a 2-diode 40 μm pixel, using 4 ms pulse, as a function of separation distance, for various pillar heights. Gray rectangle illustrates the zone within the range of observed separations of INL from the implant (<15 μm), and below the ocular safety limit for peak irradiance (<5 mW mm^{-1}). In this zone, the 10 μm pillar provides minimum sensitivity to variation in separation distance.

of high curvature due to off-axis sputtering in this direction (figure 7(D)). However, the thickness in these regions is still above 400 nm, sufficient for a high-capacitance (>1 mF cm^{-2}) interface [27].

3.3. Electric field and neural stimulation

To optimize the 3D configuration for highest spatial selectivity and lowest stimulation threshold, we modeled the retinal response to electrical stimulation using finite element modeling (see Methods). In this model, the cells are sensitive to the difference of electric potential between their soma and their axonal terminal in the middle of the IPL [28, 34].

Separation between stimulating electrode and target neurons decreases electric potential near the cell, as illustrated in figure 1(A). Pillar electrodes of appropriate height provide deeper penetration of electric field into the INL, as shown in figure 1(B). Figure 8(A) displays a simulation for a 30 μm tall pillar with 30 μm thick debris and 1 μA current. The electric potential was calculated relative to the middle of the IPL ($z = 82$ μm) for a 100% contrast grating pattern, i.e. alternating rows of the ON and OFF pixels. Black contours display simulation regions for which the potential exceeds the anodic or cathodic thresholds. Percent volume activation is calculated within the depicted pixel region of interest defined by the upper and lower INL boundary and pixel size. Figure 8(B) depicts the current and irradiance required for activation of more than half of the neurons in the pixel region of interest (50% volume above threshold) with a 4 ms pulse, using our 2-diode pixels of 40 μm in size. Pillars provide closer proximity to neurons, and therefore enable lower current for activation of the equivalent tissue volume, with the minimum current achieved when the pillar terminates near the bottom of the INL (5.8 μm and 17 μm separation for 10 μm and 20 μm pillars, respectively). For tall pillars, regions far below the pillar upper surface experience cathodic stimulation from the circumferential return electrode. This polarity requires greater potential difference and consequently higher irradiance compared to anodic stimulation [12]. Within the range of observed separations of INL from the implant (<15 μm), the 10 μm pillar provides minimum sensitivity to variation in the separation distance.

Figure 9 illustrates the electric potential relative to the middle of the IPL calculated for the same grating pattern, with anodic and cathodic pillar configurations (figure 9(A)) and their expected integration in the degenerate retinas (figure 9(B)). Black contours in figure 9(C) outline the stimulation threshold boundaries corresponding to activation of 50% of the INL volume per pixel. Arrows represent the current density, with magnitude normalized to the maximum in each figure. Pixels with a return electrode on top of the pillar have much lower stimulation threshold than the anodic configuration: they activate 50% of INL volume per pixel at one sixth of current: 0.10 μA versus 0.63 μA required with the active electrode on pillars. This is due to predominantly vertical orientation of electric field between the vertically aligned top and bottom electrodes, as opposed to lateral spread of the field with circumferential electrode on implant's surface.

However, the electric field is much less confined in this case: black contour covers the entire width of the 40 μm pixel, while the field in pixels with circumferential return at the base is tightly confined around the active electrode. Absence of this circumferential return allows the electric field to spread into neighboring pixels, and thereby increases pixel cross-talk and reduces the contrast of the stimulation pattern.

Activation volume in the INL as a function of current is shown in figure 9(D) for ON and OFF pixels. With return on pillars (cathodic pillar configuration), stimulation threshold is reduced to 0.10 μA. However, weak lateral confinement of electric field in such pixels results in tissue activation at lower irradiance not only in ON pixels, but also in OFF pixels (0.14 μA), resulting in very low contrast between them. Pixels with circumferential return exhibit higher threshold (0.63 μA), but much bigger difference (better contrast) between the ON and OFF pixels (3.30 μA).

4. Discussion

Prosthetic vision with high acuity requires localized stimulation of the remaining retinal neurons with sufficiently low threshold to enable activation of thousands of pixels necessary for object recognition [41] while avoiding excessive heating [42]. A critical factor for improving localization and stimulation threshold is reducing the distance between electrodes and target cells. The subretinal approach provides a unique, atraumatic means for close integration of the pillar electrodes with tissue by inducing migration of the inner retinal neurons into the 3D array (figures 4 and 5). Unlike subretinal implants, epiretinal prostheses typically exhibit large separation (tens to

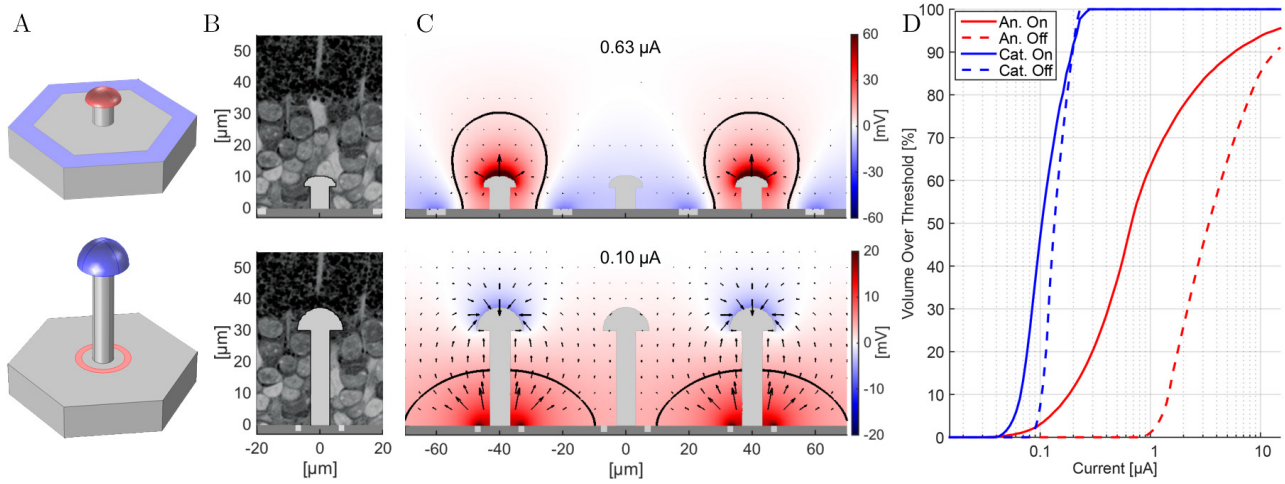

Figure 9. A row of alternating ON and OFF pixels of 40 μm in width, with anodic and cathodic pillars. (A) Pillar serving as an active (top) or return (bottom) electrode. Red and blue surfaces represent anode and cathode, respectively. (B) Diagrams of 10 μm and 35 μm tall pillar in the subretinal space. (C) Electric potential relative to the middle of IPL. Regions exceeding the stimulation threshold are below the black line. About 50% of INL volume per pixel is activated in both configurations. Arrows represent current density, with magnitude normalized to the maximum. Current spreads from anodic pillar in all directions, resulting in rapid decrease in current density, while cathodic pillars help align the electric field primarily vertically. (D) With return electrode on the pillar top (blue), stimulation threshold is significantly (≈6 fold) reduced, but the lack of circumferential return decreases lateral confinement of electric field, thereby reducing the contrast between ON and OFF pixels.

hundreds of micrometers) between electrodes and tissue due to the inability to conform to the spherical surface of the retina and lack of effective anchoring [43]. Reducing this separation requires either properly curved electrode arrays [44] or stretchable-compressible arrays to conform to spherical shape of the eye, or incorporation of 3D electrodes that would penetrate the nerve fiber layer [45], all of which are non-trivial.

Optimal design of 3D electrodes for subretinal prostheses must consider both the anatomical aspects and resulting electric field configuration in the subretinal space. Our findings regarding the anatomical integration of the pillar arrays can guide the design so that regions of maximum potential will occur in close proximity to regions of maximum cell density in the INL, while modeling of electric field helps optimize the electrode geometry for minimum thresholds and maximum spatial contrast.

The optimal pillar height depends on the electrode polarity. For anodic pillars (figure 9(A) top), the electrode surface should be placed close to or within the region of maximum density for greatest improvement in stimulation capabilities. However, the choice of pillar height must ensure that adequate amount of cell somas remain above the electrode. For these reasons, our results indicate that the 10 μm tall pillar electrode allows for the most advantageous anatomical integration: 84% of the maximum cell density, 70% INL above the pillar top, 6 μm distance to the region of maximum cell density. The 10 μm pillars also provide nearly uniform stimulation threshold over the separation distances observed after implantation (0–15 μm), as shown in figure 8. Shorter pillars do not penetrate deep enough, while much taller pillars (22 μm) reach nearly the top of INL, so very few cells remain above them for stimulation. However, optimization of the pillar height in human patients should be revisited upon OCT imaging after implantation, since the amount of subretinal debris may be larger than we observed in rats.

For cathodic pillars (figure 9(A) bottom), regions of positive potential are generated below the pillar electrode, and negative potential above it. Therefore, to hyperpolarize the cell membrane at the bottom of the soma and depolarize the cell terminals in the IPL, such pillars should end on top of INL ($h \approx 30$ μm). We have demonstrated previously that sufficiently tall pillars allow for complete migration of the INL into the inter-pillar space [15]. Cathodic pillars with active electrode ring at the bottom align electric field between two electrodes vertically (figure 9(C)), producing a larger potential drop along the vertically-aligned bipolar cells, thereby increasing the activation volume and reducing stimulation thresholds by a factor of 6, compared to pixels with an active electrode on pillars and circumferential return at the base (figure 9(D)). However, since this configuration allows for high cross-talk between neighboring pixels, it is less desirable for a high-resolution prosthesis. As can be seen in figure 9(C), cathodic pillar reaching the IPL may produce sufficiently strong electric field to induce selective depolarization of the axonal terminals, based on their stratification, leading to some selectivity in stimulation between the ON and OFF bipolar cells. Similarly, the electric field of relatively large (50 μm) monopolar electrodes penetrates sufficiently deep into the retina, creating a different trans-cellular potential in the ON and OFF cells terminating at different depth of the IPL [46]. Flat pixels or short anodic pillars with 10 μm diameter active electrode and local return cannot do that since the high electric field is localized in the INL, while the field is very weak in the IPL (top row in figure 9(C)). Therefore, selectivity in stimulation could be achieved in this case only if cell somas would be stratified in the INL, for which there is no indication in the literature.

For all subretinal implants, effective anatomical integration with the retina requires precise, atraumatic surgical procedures. Glial encapsulation in response to trauma isolates the electrodes, thereby preventing injection of sufficient current into the target cell layer. To prevent injury, surgeons must take care not to catch the detached retina on a pillar during implantation. While minor gliosis can be bypassed by the pillar structures, serious trauma may result in complete encapsulation of the device regardless of pillar height. Injection of viscoelastic material within the subretinal space prior to implantation helps stabilize the bleb and prevent such retinal injuries. Further improvement can be made by encapsulating the implant with a biodegradable material that fills in the inter-pillar space prior to implantation, or by utilizing pillars with smooth edges, as in our electroplated electrodes.

Previous studies with dummies of subretinal prostheses made of SU-8 polymer revealed large separation distances between electrodes and target tissue, ranging from 15 μm to 30 μm [40]. Such separation would require pillars of comparable height, to significantly improve stimulation capabilities compared to planar arrays (figure 8). However, the current study revealed that improved surgical procedures and the use of silicon arrays yield much smaller separation distances ($<$15 μm), thereby requiring shorter pillars for optimal placement within the INL. The decrease in stimulation thresholds reported in this work is therefore not as great as expected from the previous anatomical data and tall pillars. However, the human degenerated retina in late retinitis pigmentosa and age-related macular degeneration displays a wide variability in reorganization, with high degree of fibrosis in some cases [47, 48], which may necessitate taller pillars. In addition to improved proximity, the dome-shaped pillars increase the electrode surface area and the associated safe charge injection limits, critical for safe and stable performance and high dynamic range of stimulation.

Results of this study additionally suggest another electrode configuration for direct stimulation of the retinal ganglion cells using very tall pillars, which would terminate at the top of the IPL. In this location, stimulation of RGCs might be achieved without axonal stimulation—a major problem in epiretinal approach [10]. Axonal stimulation results from electric field gradient along the axon, which is reduced in this configuration due to placement of the electrode below cell soma—away from the axons. It can be further reduced by placing a thin return electrode on top of the inner limiting membrane (ILM), right above the nerve fiber layer. This electrode ensures that electric field between the top of the pillar and the electrode above ILM is a vertical dipole, which traverses the RGC layer and terminates on the electrode perpendicular to its surface, assuming equipotential boundary condition on metal, with no lateral component near the nerve fiber layer. This return electrode can be floating, i.e. with no wires attached, and will be connected to the remote return electrode by low impedance conduction through the ocular medium. Integration of the implant within the subretinal space will also help stabilize the device with respect to the RGC layer, unlike the poorly-attached epiretinal arrays. If the subretinal implant includes the light sensors, the floating return electrode above the epiretinal surface should be transparent, i.e. having either a transparent conductive coating, such as ITO, or being made of a fine mesh of thin wires. Our current results with 22 μm pillars and previously published results with 70 μm pillars [15] demonstrate that such pillars penetrate into the retina without significant gliosis. In this configuration, the pillar sidewall has much larger surface area compared to its top, and therefore it should be insulated to ensure current flow only from the top surface.

5. Conclusions

Optimization of the 3D electrodes for subretinal prostheses include both anatomical and electrical considerations for maximum performance improvement compared to flat arrays. In RCS rats, pillars of 10 μm height provide excellent proximity of the electrode surface to cell dense regions of the INL, with majority of cells remaining above the electrode, which is ideal for anodic pillars. For human patients, the amount of subretinal debris may be larger than we observed in rats, and pillar height can be optimized based on OCT imaging after implantation of the flat arrays. Pillars penetrating to the top of INL can act as a return (cathode) with active (anode) electrode being placed at the pillar base. This electrode geometry results in activation of a larger tissue volume, with greater potential step along the vertically aligned cells, compared to active electrode on pillar and circumferential return electrode at the base. However, such arrays suffer from strong cross-talk due to reduced field confinement in absence of circumferential return. Given these results, photovoltaic arrays with pillars of 10 μm in height, having hemi-spherical SIROF-coated electrode on top, appears to be optimal for subretinal stimulation. Finally, we propose a solution to the problem of axonal activation in epiretinal stimulation by using a subretinal implant with pillars penetrating to the top of IPL for direct stimulation of the ganglion cells, where a floating thin-film electrode above the epiretinal surface ensures the absence of lateral electric field activating the axons.

Acknowledgments

We would like to thank Drs Cédric Espenel and Lydia Marie-Joubert of the Stanford Cell Sciences Imaging Facility for imaging advice, as well as Corinne Beier (University of California Santa Cruz) for helpful discussions about immunohistochemistry preparations. Supported by the National Institutes of Health (Grants R01-EY-018608, R01-EY-027786), the Department of Defense (Grant W81XWH-15-1-0009), Stanford Neurosciences Institute, and Research to Prevent Blindness. Fabrication of the silicon implants was performed at the Stanford Nanofabrication Facility (SNF) and Stanford Nano Shared Facilities (SNSF), supported by the National Science Foundation (Award ECCS-1542152).

ORCID iDs

Thomas Flores https://orcid.org/0000-0001-6753-3942

References

[1] Smith W, Assink J, Klein R, Mitchell P and Klaver C 2001 Risk factors for age-related macular degeneration: pooled findings from three continents *Ophthalmology* **108** 697–704

[2] Haim M 2002 The epidemiology of retinitis pigmentosa in Denmark *Acta Ophthalmol.* **80** 1–34

[3] Goetz G A and Palanker D V 2016 Electronic approaches to restoration of sight *Rep. Prog. Phys.* **79** 096701

[4] Zhou D D, Dorn J D and Greenberg R J 2013 The Argus® II retinal prosthesis system: an overview *IEEE Int. Conf. on Multimedia and Expo Workshops* (IEEE) pp 1–6

[5] Stingl K *et al* 2015 Subretinal visual implant alpha IMS–clinical trial interim report *Vis. Res.* **111** 149–60

[6] Lorach H *et al* 2015 Photovoltaic restoration of sight with high visual acuity *Nat. Med.* **21** 476–82

[7] Ayton L N *et al* 2014 First-in-human trial of a novel suprachoroidal retinal prosthesis *PLoS One* **9** e115239

[8] Ho A C *et al* 2015 Long-term results from an epiretinal prosthesis to restore sight to the blind *Ophthalmology* **122** 1547–54

[9] Stingl K, Bartz-Schmidt K U, Gekeler F, Kusnyerik A, Sachs H and Zrenner E 2013 Functional outcome in subretinal electronic implants depends on foveal eccentricity *Investigative Ophthalmol. Vis. Sci.* **54** 7658–65

[10] Grosberg L E *et al* 2017 Activation of ganglion cells and axon bundles using epiretinal electrical stimulation *J. Neurophysiol.* **118** 1457–71

[11] Nanduri D, Fine I, Horsager A, Boynton G M, Humayun M S, Greenberg R J and Weiland J D 2012 Frequency and amplitude modulation have different effects on the percepts elicited by retinal stimulation *Investigative Ophthalmology Investigative Ophthalmol. Vis. Sci. Visual Science* **53** 205–14

[12] Boinagrov D, Pangratz-Fuehrer S, Goetz G and Palanker D V 2014 Selectivity of direct and network-mediated stimulation of the retinal ganglion cells with epi-, sub- and intraretinal electrode *J. Neural Eng.* **11** 026008

[13] Weitz A C, Nanduri D, Behrend M R, Gonzalez-Calle A, Greenberg R J, Humayun M S, Chow R H and Weiland J D 2015 Improving the spatial resolution of epiretinal implants by increasing stimulus pulse duration *Sci. Transl. Med.* **7** 318ra203

[14] Wilke R G H, Moghadam G K, Lovell N H, Suaning G J and Dokos S 2011 Electric crosstalk impairs spatial resolution of multi-electrode arrays in retinal implants *J. Neural Eng.* **8** 046016

[15] Palanker D V, Vankov A, Huie P and Baccus S 2005 Design of a high-resolution optoelectronic retinal prosthesis *J. Neural Eng.* **2** S105–20

[16] Hungar K, Görtz M, Slavcheva E and Spanier G 2005 Production processes for a flexible retina implant (Eurosensors XVIII, Session C6. 6) *Sensors Actuators* A **123** 172–8

[17] Lee K W, Watanabe Y, Kigure C, Fukushima T, Koyanagi M and Tanaka T 2012 Pillar-shaped stimulus electrode array for high-efficiency stimulation of fully implantable epiretinal prosthesis *J. Micromech. Microeng.* **22** 105015

[18] Ko H and Lee S 2017 Electrical characterization of 2D and 3D microelectrodes for achieving high resolution sensing in retinal prostheses with in vitro animal experimental results *Microsyst. Technol.* **23** 473–81

[19] Palanker D V, Huie P, Vankov A, Aramant R, Seiler M, Fishman H, Marmor M and Blumenkranz M 2004 Migration of retinal cells through a perforated membrane: implications for a high-resolution prosthesis *Investigative Ophthalmol. Vis. Sci.* **45** 3266–70

[20] Mathieson K *et al* 2012 Photovoltaic retinal prosthesis with high pixel density *Nat. Photon.* **6** 391–7

[21] Djilas M *et al* 2011 Three-dimensional electrode arrays for retinal prostheses: modeling, geometry optimization and experimental validation *J. Neural Eng.* **8** 046020

[22] Bendali A *et al* 2015 Synthetic 3D diamond-based electrodes for flexible retinal neuroprostheses: model, production and in vivo biocompatibility *Biomaterials* **67** 73–83

[23] Lee S, Ahn J H, Seo J M, Chung H and Cho D I 2015 Electrical characterization of 3D Au microelectrodes for use in retinal prostheses *Sensors* **15**

[24] Fujisawa T, Noda T, Hayashi M, Kobe R, Tashiro H, Takehara H, Sasagawa K, Tokuda T, Wu C Y and Ohta J 2016 Performance improvement of a micro-stimulus electrode for retinal prosthesis by introducing a high-performance material and a three-dimensional structure *Sens. Mater.* **28** 1303–15

[25] Weidlich S, Krause K J, Schnitker J, Wolfrum B and Offenhäusser A 2017 MEAs and 3D nanoelectrodes: electrodeposition as tool for a precisely controlled nanofabrication *Nanotechnology* **28** 095302

[26] Boinagrov D, Lei X, Goetz G, Kamins T I, Mathieson K, Galambos L, Harris J S and Palanker D V 2016 Photovoltaic pixels for neural stimulation: circuit models and performance *IEEE Trans. Biomed. Circuits Syst.* **10** 85–97

[27] Cogan S F, Plante T D and Ehrlich J 2004 Sputtered iridium oxide films (SIROFs) for low-impedance neural stimulation and recording electrodes *Engineering in Medicine and Biology Society, 2004. IEMBS'04. 26th Annual Int. Conf. of the IEEE* (Norwood, MA: EIC Laboratories, Inc.) pp 4153–6

[28] Flores T, Goetz G, Lei X and Palanker D V 2016 Optimization of return electrodes in neurostimulating arrays *J. Neural Eng.* **13** 036010

[29] Lorach H *et al* 2015 Development of animal models of local retinal degeneration *Investigative Ophthalmol. Vis. Sci.* **56** 4644–52

[30] Lorach H, Goetz G, Mandel Y, Lei X, Kamins T I, Mathieson K, Huie P, Dalal R, Harris J S and Palanker D V 2015 Performance of photovoltaic arrays in-vivo and characteristics of prosthetic vision in animals with retinal degeneration *Vis. Res.* **111** 142–8

[31] Schindelin J *et al* 2012 Fiji: an open-source platform for biological-image analysis *Nat. Methods* **9** 676–82

[32] Harnois C, Bodis-Wollner I and Onofrj M 1984 The effect of contrast and spatial frequency on the visual evoked potential of the hooded rat *Exp. Brain Res.* **57**

[33] Wang L *et al* 2012 Photovoltaic retinal prosthesis: implant fabrication and performance *J. Neural Eng.* **9** 046014

[34] Werginz P and Rattay F 2016 The impact of calcium current reversal on neurotransmitter release in the electrically stimulated retina *J. Neural Eng.* **13** 046013

[35] Boinagrov D, Loudin J and Palanker D V 2010 Strength-duration relationship for extracellular neural stimulation: numerical and analytical models *J. Neurophysiol.* **104** 2236–48

[36] Jensen R J, Ziv O R and Rizzo J F III 2005 Thresholds for activation of rabbit retinal ganglion cells with relatively large, extracellular microelectrodes *Investigative Ophthalmol. Vis. Sci.* **46** 1486–96

[37] Karwoski C J, Proenza L M and Frambach D A 1986 Determination of resistivity and transcellular current flow in frog retina *Ann. New York Acad. Sci.* **481** 365–8

[38] Wang B and Weiland J D 2015 Resistivity profiles of wild-type, rd1, and rd10 mouse retina *2012 Annual Int. Conf. of the IEEE Engineering in Medicine and Biology Society* (IEEE) pp 1650–3

[39] Loizos K, RamRakhyani A K, Anderson J, Marc R and Lazzi G 2016 On the computation of a retina resistivity profile for applications in multi-scale modeling of electrical stimulation and absorption *Phys. Med. Biol.* **61** 4491–505
[40] Butterwick A, Huie P, Jones B W, Marc R E, Marmor M and Palanker D V 2009 Effect of shape and coating of a subretinal prosthesis on its integration with the retina *Exp. Eye Res.* **88** 22–9
[41] Jung J H, Aloni D, Yitzhaky Y and Peli E 2015 Active confocal imaging for visual prostheses *Vis. Res.* **111** 182–96
[42] Lorach H, Wang J, Lee D Y, Dalal R, Huie P and Palanker D V 2016 Retinal safety of near infrared radiation in photovoltaic restoration of sight *Biomed. Opt. Express* **7** 13
[43] Ahuja A K, Yeoh J, Dorn J D, Caspi A, Wuyyuru V, McMahon M J, Humayun M S, Greenberg R J, daCruz L and Argus II Study Group 2013 Factors affecting perceptual threshold in Argus II retinal prosthesis subjects *Transl. Vis. Sci. Technol.* **2** 1–15
[44] Scribner D *et al* 2007 A Retinal Prosthesis Technology Based on CMOS Microelectronics and Microwire Glass Electrodes *IEEE Trans. Biomed. Circuits Syst.* **1** 73–84
[45] Gross Y and Vaingast S 2012 Retinal prosthesis *US Patent* 8,150,526
[46] Werginz P, Benav H, Zrenner E and Rattay F 2015 Modeling the response of ON and OFF retinal bipolar cells during electric stimulation *Vis. Res.* **111** 170–81
[47] Milam A H, Li Z Y and Fariss R N 1998 Histopathology of the human retina in retinitis pigmentosa *Prog. Retinal Eye Res.* **17** 175–206
[48] Jones B W, Pfeiffer R L, Ferrell W D, Watt C B, Tucker J and Marc R E 2016 Retinal remodeling and metabolic alterations in human AMD *Frontiers Cell. Neurosci.***10**